

The Binary Fraction of Red Supergiants in the Magellanic Clouds

Min Dai,^{1,2} Shu Wang^{3*} and Biwei Jiang^{1,2†}

¹*School of Physics and Astronomy, Beijing Normal University, Beijing 100875, People's Republic of China*

²*Institute for Frontiers in Astronomy and Astrophysics, Beijing Normal University, Beijing 102206, People's Republic of China*

³*CAS Key Laboratory of Optical Astronomy, National Astronomical Observatories, Chinese Academy of Sciences, Beijing 100101, People's Republic of China*

Accepted 2025 April 03. Received 2025 April 03; in original form 2024 October 23

ABSTRACT

Red supergiants (RSGs), as the descendants of OB-type stars and the progenitors of supernovae, provide crucial insights into the evolution of massive stars, particularly in binary systems. Previous studies show that the binary fraction of RSGs ($\approx 15\% - 40\%$) is significantly lower than that of their predecessors ($\approx 50\% - 70\%$). In this work, we investigate the binary fraction of RSGs with the recently selected largest samples of 4695 and 2097 RSGs in the Large Magellanic Cloud (LMC) and Small Magellanic Cloud (SMC), respectively. The binary system with a hot companion (O-, B- and A-type star) is identified by detecting the ultraviolet (UV) excess in the observed spectral energy distribution (SED) ranging from ultraviolet to mid-infrared after subtracting the model SED of RSG since RSGs are very weak in the UV band. It is found that the lower limit of binarity is $30.2\% \pm 0.7\%$ and $32.2\% \pm 1\%$ in the LMC and SMC, respectively. If the sample is limited to luminous RSGs with $\log L/L_{\odot} > 4.0$, the binary fraction becomes $26.6\% \pm 1.1\%$ and $26.4\% \pm 1.7\%$ in the LMC and SMC, respectively. The derived binary fraction is valid in the range of $\sim 2.3 < \log P/[d] < \sim 8$. Our study suggests that roughly one-third of massive stars host a third companion within $\sim 30,000$ AU. In addition, 15 RSGs are also identified as binary via HST/STIS spectra, and a handful of the binaries identified by the SED fitting are confirmed by their light curve and radial velocity dispersion. The stellar parameters of the companions, i.e. T_{eff} , R , L and $\log g$, are calculated by model fitting.

Key words: Stars: late-type – Stars: massive – Supergiants – Binaries: general – Magellanic Clouds

1 INTRODUCTION

Red supergiants (RSGs) are massive stars located in the upper right of the Hertzsprung-Russell (H-R) diagram. The initial mass of RSGs is about between $6.1 - 30 M_{\odot}$ (Yang et al. 2024). As the evolved descendants of OB-type main-sequence stars, RSGs have low effective temperatures ($T_{\text{eff}} \approx 3500 - 4500$ K), very high luminosities ($L/L_{\odot} \approx 4 - 5.8$) and large radii ($R \approx 1500 R_{\odot}$) (Levesque et al. 2005; Massey et al. 2007b, 2008; Wittkowski et al. 2012; Davies et al. 2013; Massey & Evans 2016).

Most massive stars are found in binary or in multiple star system (Mason et al. 1998; García & Mermilliod 2001; Sana et al. 2012, 2014; Kobulnicky et al. 2014). The binary fraction of OB-type stars in the period range $0 \lesssim \log P/[d] \lesssim 3$ was determined to be at least $\sim 50\% - 70\%$ (Gies 2008; Sana et al. 2012, 2013; Dunstall et al. 2015; Shenar et al. 2022; Shenar 2024). However, previous studies found the binary fraction of RSGs $\approx 15\%$ to 40% , employing diverse methodologies that correspond to detecting different orbital period ranges, which will be discussed in subsequent sections (Patrick et al. 2019, 2020; Neugent et al. 2020; Neugent 2021; Dorda & Patrick 2021; Patrick et al. 2022), significantly lower than their progenitors. RSGs are not only descendants of OB-type stars, but also the progenitors of certain types of supernovae. RSGs with masses between about 8 and $25 M_{\odot}$ will explode as Type II-P supernovae, as pre-

dicted by single star models (Woosley & Heger 2006; Groh et al. 2013). The evolution of RSG in a binary system can be classified into two distinct categories. If the orbital period is greater than 1,500 days (very wide binary systems, Sana et al. 2012), the evolution is identical to that of a single star. However, many Type II supernova progenitors undergo mass exchange before exploding (Zapartas et al. 2019), and interacting binaries may be the key to understanding the diversity of Type II supernova light curves (Eldridge et al. 2018). The study of RSG binary populations can contribute to the development of evolutionary models of massive stars.

Two methods are generally used to study the binary fraction of RSGs. One way is to analyze the variability of radial velocity (RV). In this way, Patrick et al. (2019) derive that the upper limit of binary fraction of RSGs is 30% in a sample of 17 RSGs in the 30 Doradus region of the Large Magellanic Cloud (LMC), with the orbital period range $3.3 \leq \log P/[d] \leq 4.3$. Later, Patrick et al. (2020) report a binary fraction of $30 \pm 10\%$ in a sample of 15 RSGs in the NGC 330 region of the Small Magellanic Cloud (SMC), with the orbital period range $2.3 \leq \log P/[d] \leq 4.3$. Dorda & Patrick (2021) find a minimum binary fraction of $14 \pm 5\%$ in a sample of 51 cool supergiants (CSGs) in the LMC and of $15 \pm 4\%$ from a sample of 72 CSGs in the SMC, with the orbital period range $2.8 \leq \log P/[d] \leq 3.6$. The other way is to detect the blue-star spectral features (BSSFs) from spectra (e.g., Neugent et al. 2018). Neugent et al. (2020) further develop the BSSFs method. They use a machine-learning method based on k -nearest-neighbor algorithm (k -NN) with U , B , V , and I photometry to classify stars as single or binary. They find the bi-

* E-mail: shuwang@nao.cas.cn

† E-mail: bjiang@bnu.edu.cn

nary fraction of RSGs = $19.5^{+7.5}_{-6.7}\%$ with a sample of 1820 RSGs in the LMC. The period sensitivity range by the single-epoch spectroscopy and photometric identification is not explicitly mentioned in the respective articles. Afterwards, Neugent (2021) apply a similar method to a sample of 1909 and 1702 RSGs in M31 and M33, respectively. They find that the binary fraction of RSGs in M33 shows a strong dependence on galactocentric distance ($41.2^{+12}_{-7.3}\%$ at inner regions; $15.9^{+8.6}_{-1.9}\%$ at outer regions) and the binary fraction of RSGs = $33.5^{+8.6}_{-5.0}\%$ in M31.

In addition to the two methods mentioned above, Patrick et al. (2022) make use of the fact that the brightness of RSGs is significantly fainter than that of main-sequence B-type stars in the near- and far-UV (NUV and FUV, respectively) to distinguish binary RSGs from single. They report a binary fraction of $18.8 \pm 1.5\%$ in a sample of 560 RSGs in the SMC by using the Ultraviolet Imaging Telescope (UVIT) FUV ($0.172 \mu\text{m}$) photometry, with the orbital period range $3 \leq \log P/[\text{d}] \leq 8$. In brief, a RSG is regarded as in a binary once detected by UVIT at $0.172 \mu\text{m}$. Based on the same rule that the detection of UV excess is an indicator of early-type star companion, this work attempts to identify the binary RSGs in the LMC and SMC by fitting the spectral energy distribution (SED) of RSGs in the MCs. While RV method exhibits constraints in its detectable orbital period range (e.g., $\log P/[\text{d}] \leq 4.3$), previous photometric studies have been limited by incomplete datasets. We therefore employ multi-band photometric data to investigate the binary fraction of RSGs in the MCs. The UV photometry is taken from several observations including SMASH, HST, GALEX, *Swift*/UVOT, XMM-OM and SMSS besides UVIT. Furthermore, the sample of RSGs is recently renewed significantly based on the astrometric measurements and new method to exclude the foreground dwarfs stars. From the SED fitting, we are able to identify the RSG binary with hot companions (e.g. A-, B-, O-type stars). The principle idea of this method is that the fluxes in the red and near-infrared (NIR) bands is dominated by the RSG, while in the UV bands, it is dominated by the hot companion.

This paper is structured as follows. In Section 2, we describe the datasets for constructing SEDs and the sample of RSGs in the MCs. The methods for obtaining the binary fraction of RSGs and the parameters of both RSGs and their companions are presented in Section 3. In Section 4, we compare our results with previous works, the distributions of our samples in the color-color diagrams, extra evidence of identifying binaries, and the limitations of this study. Finally, the main conclusions are presented in Section 5.

2 DATA AND SAMPLE

2.1 Data

The photometric data from UV to infrared (IR) are collected to construct the SED. The surveys used include: (1) X-ray Multi-Mirror Mission Optical Monitor (XMM-OM, Jansen et al. 2001; Mason et al. 2001), (2) UltraViolet and Optical Telescope (UVOT, Gehrels 2004; Roming et al. 2005), (3) UV Imaging Telescope (UVIT, Kumar et al. 2012; Hutchings 2014), (4) Hubble Space Telescope (HST), (5) Galaxy Evolution Explorer (GALEX, Morrissey et al. 2005, 2007), (6) the Survey of the Magellanic Stellar History (SMASH, Nidever et al. 2017), (7) the SkyMapper Southern Survey (SMSS, Wolf et al. 2018), (8) Gaia (Gaia Collaboration et al. 2023), (9) the Two Micron All Sky Survey (2MASS, Skrutskie et al. 2006), (10) the Wide-field Infrared Survey Explorer (WISE, Wright et al. 2010), and (11) Spitzer Space Telescope (Spitzer, Werner et al. 2004). All filters information used in this work are presented in Table 1. Be-

sides, the spectroscopic data are collected from the Apache Point Observatory Galactic Evolution Experiment (APOGEE, Majewski et al. 2017), Gaia low-resolution blue/red prism photometer BP/RP mean spectra (XP spectra, Montegriffo et al. 2023) and the Hubble Space Telescope Imaging Spectrograph (HST/STIS). The brief introduction to these projects are following.

2.1.1 Photometry

XMM-OM is the optical monitor of the *XMM-Newton* space observatory. It provides photometries in UVW2 ($0.2 \mu\text{m}$), UVM2 ($0.23 \mu\text{m}$), UVW1 ($0.29 \mu\text{m}$), *U*, *B* and *V* (Jansen et al. 2001; Mason et al. 2001). The PSF FWHM aperture size is $\sim 2''$ in the UV bands. The photometric data are taken from XMM-OM serendipitous UV source survey catalogue 5.0 (Page et al. 2012).

Swift/UVOT is a telescope of *Swift* mission. It provides photometries in UVW2 ($0.21 \mu\text{m}$), UVM2 ($0.22 \mu\text{m}$), UVW1 ($0.28 \mu\text{m}$), *U*, *B* and *V* (Gehrels 2004; Roming et al. 2005). The PSF FWHM aperture size is $\sim 0.9''$ at $0.35 \mu\text{m}$. The photometric data are taken from the serendipitous UV source catalogs (Yershov 2014).

UVIT is a telescope of ASTROSAT mission. It provides 17 bands for FUV ($130 - 180 \text{ nm}$), NUV ($200 - 300 \text{ nm}$) and blue-visible ($320 - 550 \text{ nm}$) (Kumar et al. 2012; Hutchings 2014; Singh et al. 2014). The PSF FWHM aperture size is $\sim 1.40''$ in F172M. (Piridi et al. 2024) Part of the FUV and NUV photometric data are taken from Patrick et al. (2022) and Devaraj et al. (2023).

HST is a 2.4-m space telescope. The UV ($\lambda < 0.38 \mu\text{m}$) photometric data are taken from Hubble Source Catalog (HSC¹). The PSF FWHM aperture size of WFC3/UVIS is $\sim 0.075''$ in the UV bands. The criterion of “Flags = 0” is adopted to ensure the data quality (Whitmore et al. 2016).

GALEX is an all-sky survey using a 50-cm telescope to provide NUV ($0.23 \mu\text{m}$) and FUV ($0.15 \mu\text{m}$) photometry (Morrissey et al. 2005, 2007). The photometric data are taken from the revised catalog of GALEX ultraviolet sources (GUVcat_AIS, Bianchi et al. 2017). The spatial resolutions (FWHM) are $4.3''$ and $5.3''$ in the FUV and NUV, respectively. The criteria of “largeobjsize = 0”, $13.73 < \text{FUV} < 19.9 \text{ mag}$ and $13.85 < \text{NUV} < 20.8 \text{ mag}$ are adopted to ensure the data quality.

SMASH is a survey project by using the dark energy camera on the NOAO Blanco 4-m telescope at the Cerro Tololo Inter-American Observatory (CTIO) to observe the Magellanic Clouds and their periphery. It observes about 480 square degrees of sky with a depth down to 24th mag in *u*, *g*, *r*, *i*, *z* (Nidever et al. 2017). The PSF FWHM aperture size is $\sim 1''$ in *u* and *g* bands. The *u* and *g* band photometric data are taken from data release 2 (DR2) (Nidever et al. 2021), and the criterion of photometric error $< 0.05 \text{ mag}$ is adopted to ensure the data quality.

SMSS is a southern sky survey by using the 1.3-m SkyMapper telescope at Siding Spring Observatory in Australia in six bands, i.e. *u*, *v*, *g*, *r*, *i*, *z* (Wolf et al. 2018). The photometric accuracy of the DR2 is 1% in *u* and *v*, and 0.7% in *griz* (Onken et al. 2019). The median PSF FWHM aperture size is $3.1''$, $2.9''$, $2.6''$, $2.4''$, $2.3''$ and $2.3''$ in the *u*, *v*, *g*, *r*, *i* and *z* bands. The criteria of “x_flags = 0” and “x_nimaf flags = 0” are adopted to ensure the data quality. Besides, the filters of SMSS *u* and SMASH *u* are similar. For the sources overlapped with SMASH *u*, a linear fit is performed between SMSS *u* and SMASH *u* by using the RANSAC algorithm of the scikit-learn package. The observations of SMSS *u* and *v* with 1σ outliers are

¹ <https://catalogs.mast.stsci.edu/hsc>

removed since the SMSS u band has a brighter limiting magnitude and some known issues described by [Onken et al. \(2019\)](#).

The third Gaia data release, Gaia DR3, provides broadband photometry in the G , G_{BP} and G_{RP} bands for more than 1.5 billion sources, radial velocity (RV) measurements for more than 33 million bright stars, and low-resolution blue/red prism photometer BP/RP mean spectra for about 220 million sources ([Gaia Collaboration et al. 2023](#)). The spatial resolutions of Gaia is $\sim 1.5''$ ([Gaia Collaboration et al. 2021](#)). The G_{BP} and G_{RP} brightness are used in constructing SEDs, and the RV data are used in excluding foreground dwarf stars and identifying binaries.

2MASS is an all-sky survey that provides photometry in the NIR J , H , and K_S bands. Its 10σ point-source detection depths are better than 15.8, 15.1, and 14.3 mag in the three bands, respectively ([Skrutskie et al. 2006](#)). The median PSF FWHM aperture size is $\sim 3''$ in the J , H , and K_S bands. The J , H , and K_S data are taken from 2MASS all-sky point-source catalog ([Cutri et al. 2003](#)).

WISE is an all-sky survey in four infrared bands in W1, W2, W3 and W4 ([Wright et al. 2010](#)). The angular resolution is $6.1''$, $6.4''$, $6.5''$ and $12.0''$ in the W1, W2, W3 and W4 bands. The photometric data are taken from the AllWISE catalog ([Cutri et al. 2021](#)).

Spitzer is an infrared space telescope. It carried three infrared instruments, the Infrared Array Camera (IRAC), the Infrared Spectrograph (IRS), and the MIPS ([Werner et al. 2004](#)). The spatial resolution is $\sim 2''$ in IRAC bands. The four IRAC bands and [24] band of MIPS data are taken from Spitzer Science Center & Infrared Science Archive ([2021](#)).

2.1.2 Spectroscopic Data

APOGEE is a spectroscopic survey of the Sloan Digital Sky Survey (SDSS) project. It produces the high-resolution ($R \sim 22,500$) infrared ($1.51\text{--}1.70\ \mu\text{m}$) spectra by using the 2.5-m Sloan Telescope and du Pont Telescope ([Gunn et al. 2006](#); [Majewski et al. 2017](#); [Wilson et al. 2019](#)). The stellar parameters (T_{eff} and RV) are taken from DR17 ([Abdurro'uf et al. 2022](#)).

The Gaia XP spectra are a low-resolution ($\lambda/\Delta\lambda = 30 - 100$) data product released by Gaia DR3 ([Carrasco et al. 2021](#)). The XP spectra covers the 330 nm to 1050 nm wavelength range. The XP spectra are used only in the range of 400 to 900 nm because of systematic effects at $\lambda < 400$ nm and $\lambda > 900$ nm ([Montegriffo et al. 2023](#)). The XP spectra of possibly poor quality are omitted by using a 3σ criterion, where the σ is calculated by comparing the photometry of G_{BP} and G_{RP} from Gaia DR3 with synthetic photometry of G_{BP} and G_{RP} derived from XP spectra. The calibrated spectra are obtained by using GaiaXPpy² ([Ruz-Mieres & zuzannakr 2023](#)). In the process of fitting the companion SED, the XP spectra are used to replace the photometry in the UVOT/ BV bands, XMM-OM/ BV bands, SMASH/ g band, SMSS/ gri bands and APASS all bands.

HST spectra are collected from Space Telescope Imaging Spectrograph (STIS). The HST/STIS grating spectrum used in this work is named G230LB, and it covers the wavelength from $0.17\ \mu\text{m}$ to $0.31\ \mu\text{m}$, and has a spectroscopic resolution of $R \sim 700$ ([Medallan et al. 2023](#)).

2.2 The RSG Samples

Until 2020, only a few hundred RSGs have been identified in the LMC and SMC ([Feast et al. 1980](#); [Catchpole & Feast 1981](#); [Wood et al. 1983](#); [Pierce et al. 2000](#); [Massey 2002](#); [Massey & Olsen 2003](#); [Yang & Jiang 2011, 2012](#); [Neugent et al. 2012](#); [González-Fernández et al. 2015](#)). With updated data and methods for identifying RSGs in the MCs, the number of RSGs has increased by orders of magnitude in recent years. [Yang et al. \(2020, 2021\)](#) identify 2974 (LMC) and 1239 (SMC) RSGs by using an astrometric solution from Gaia/DR2 and multiband color–magnitude diagrams (CMDs). [Wang & Chen \(2023\)](#) construct a spectroscopic sample with 1073 (LMC) and 398 (SMC) RSGs by using astrometric data from Gaia and spectroscopic data from APOGEE. [Neugent et al. \(2020\)](#) report 4090 RSGs with $\log L/L_{\odot} > 3.5$ in the LMC by using astrometric data from Gaia/DR2 and CMD. [Massey et al. \(2021\)](#) identify 1745 RSGs in the SMC by using the same method as [Neugent et al. \(2020\)](#).

We use the sample of [Ren et al. \(2021\)](#) which includes 4823 and 2138 RSGs in the LMC and SMC, respectively. They use the updated astrometric data (Gaia/EDR3) and intrinsic NIR color–color diagram (CDD) to remove foreground dwarfs, and identify RSGs in the intrinsic CMD. The sample of [Ren et al. \(2021\)](#) contains 77% (LMC) and 74% (SMC) of the RSGs from [Yang et al. \(2020, 2021\)](#), 93% (LMC) and 95% (SMC) of the RSGs from [Wang & Chen \(2023\)](#), 95% (LMC) of the RSGs from [Neugent et al. \(2020\)](#), and 91% (SMC) of the RSGs from [Massey et al. \(2021\)](#). Compared to previous samples, this one is larger in number or purer. In order to further purify the sample, 128 (LMC) and 41 (SMC) foreground dwarfs are removed by adopting the criteria with $RV < 200\ \text{km s}^{-1}$ for the LMC and $RV < 95\ \text{km s}^{-1}$ for the SMC, where the RV values are taken from the APOGEE or Gaia catalog. Finally, a sample of 4695 and 2097 RSGs in the LMC and SMC is used in further analysis.

A radius of $1''$ is adopted to cross-match the RSG sample with photometric and spectroscopic catalogs listed in Section 2.1. The number of stars cross-matched with each catalog is as follows:

- For SMASH data, 6265 RSGs (92.24%) in the u band.
- For XMM-OM data, 71 (1.05%), 90 (1.32%), 641 (9.43%) and 106 (1.56%) RSGs in the UVW2, UVM2, UVW1 and U band, respectively.
- For *Swift*/UVOT data, 32 (0.47%), 8 (0.12%), 46 (0.68%) and 83 (1.22%) RSGs in the UVW2, UVM2, UVW1 band U band, respectively.
- For UVIT data, 87 (1.28%) and 5 RSGs (0.07%) in the F172M and N279N band, 4 RSGs (0.06%) in the F154W and F169M band, 3 RSGs (0.04%) in the N219M, N245M and N263M band, respectively.
- For HST data, 1 (0.01%), 18 (0.27%), 22 (0.32%), 2 (0.03%), 29 (0.43%), 57 (0.84%), 6 (0.09%) and 3 (0.04%) RSGs in the F170W, F225W, F275W, F280N, F300W, F336W, F343N and F373N band, respectively.
- For GALEX data, 5 RSGs (0.07%) in the FUV and NUV band.
- For SMSS data, 347 (5.11%), 811 (11.94%), 3217 (47.36%) RSGs in the u , v and z band.
- For Gaia data, 6755 (99.46%) and 6756 (99.47%) RSGs in the G_{BP} and G_{RP} band.
- For 2MASS data, 6792 RSGs (100%) in the J , H and K_S band.

3 METHOD AND RESULT

3.1 Fitting the SED of RSGs

The observational SED of RSG is fitted to retrieve the stellar parameters and form the basis to judge whether the UV excess exists. The

² <https://gaia-dpci.github.io/GaiaXPpy-website/>

model spectra are taken from the synthetic stellar spectra of Lejeune et al. (1997; hereafter L97). The L97 library covers the T_{eff} from 2500 K to 50,000 K, $\log g$ from -1.02 to 5.0, and $[M/H]$ from -3.5 dex to 1.0 dex. In order to improve the fitting precision, the interval of T_{eff} is narrowed from 250 K down to 50 K by interpolation.

The interstellar extinction correction is necessary to the photometric results at this step. Due to the red colors of RSGs, the effective wavelength λ_{eff} of the photometric band can be quite different from the claimed one generally for an A0-type star, in particular in the UV bands. Thus λ_{eff} is first calculated at the typical stellar parameters of RSGs, specifically $T_{\text{eff}} = 4000$ K, $\log g = 0$, and $[M/H] = -0.5$ for the LMC, $[M/H] = -1.0$ for the SMC,

$$\lambda_{\text{eff}} \equiv \frac{\int \lambda T(\lambda) S(\lambda) d\lambda}{\int T(\lambda) S(\lambda) d\lambda}, \quad (1)$$

where $T(\lambda)$ is the filter transmission, and $S(\lambda)$ is the stellar model spectrum. To obtain A_λ , $E(V-I)$ is taken from the OGLE extinction map by Skowron et al. (2021), and then converted to A_λ with the extinction law by Wang & Chen (2023). The fitting is later performed to the SED after extinction correction.

Since the flux at the wavelength shorter than $0.75 \mu\text{m}$ may be affected by the companion and the flux at the wavelength longer than $2.5 \mu\text{m}$ may be affected by circumstellar dust, the SED of RSG component is fitted only to the observations at the wavelength between $0.75 \mu\text{m}$ to $2.5 \mu\text{m}$, including Gaia G_{RP} , SMSS z , and 2MASS J , H , K_s . To assess the goodness of fitting, the reduced χ^2 for each star is calculated as

$$\frac{\chi^2}{\text{dof}} = \frac{\sum_{j=1}^{N_{\text{obs}}} [F_\nu(\lambda_j)^{\text{mod}} - F_\nu(\lambda_j)^{\text{obs}}]^2 / w(\lambda_j)^2}{N_{\text{obs}} - N_{\text{para}}}, \quad (2)$$

where $F_\nu(\lambda_j)^{\text{mod}}$ and $F_\nu(\lambda_j)^{\text{obs}}$ are the model and the observed flux after correcting the extinction, respectively. $F_\nu(\lambda_j)^{\text{mod}}$ is calculated by

$$F_\nu(\lambda_j)^{\text{mod}} \equiv \frac{\int T(\lambda) S(\lambda) d\lambda}{\int T(\lambda) d\lambda}. \quad (3)$$

The weight is defined as $w(\lambda_j) = [F_\nu(\lambda_j)^{\text{mod}} + F_\nu(\lambda_j)^{\text{obs}}]/2$ to eliminate the effect caused by the large flux difference between various bands. N_{obs} is the number of observational data and N_{para} is the model parameter. Indeed, only T_{eff} is fitted as $\log g$ and $[M/H]$ are set to be constant for one galaxy, i.e. $\log g = 0^3$, $[M/H] = -0.5$ (LMC) or $[M/H] = -1.0$ (SMC). The influence of various parameters will be discussed later and it's small. With the T_{eff} fitted, stellar radius (R) and luminosity (L) are calculated by

$$R = d \sqrt{\frac{F_\nu(\lambda)^{\text{obs}}}{F_\nu(\lambda)^{\text{mod}}}}, \quad (4)$$

$$L = 4\pi R^2 F, \quad (5)$$

where d is the distance of the MCs, and F is the integrated flux of model spectrum. The distance modulus = 18.49 mag for the LMC and 18.94 mag for the SMC are adopted to calculate the d (de Grijs et al. 2014; Crandall & Ratra 2015). The stellar parameters derived from the SED fitting are summarized in Table 2.

Figure 1 shows the distribution of the reduced χ^2 for fitting the SED of RSGs. The red dashed line in Figure 1 denotes the critical value of $\chi^2 = 0.00748$ at the 95% confidence level. A reserved sample

of 4390 and 2063 RSGs in the LMC and SMC is selected by removing the objects with $\chi^2 > 0.00748$. It is worth noting that we check the SED fitting diagrams of all stars with reduced $\chi^2 > 0.00748$ (305 in the LMC, 34 in the SMC), and find that 14% of them show significant excess UV flux. This means that a small number of RSG binaries may be missed in this work. Two examples are displayed in Figure 2. The left panel is the result of a single RSG star with a reduced χ^2 around the median value, while the right panel is that of a candidate binary RSG with a reduced χ^2 greater than the 95% confidence value.

The typical uncertainty of stellar parameters is estimated by the MCMC method for one star, 2MASS J04494147-6904402, whose photometric errors in J , H , K_s are around the median value of all sample stars. A total of 5000 SED fitting is performed to the observational SED that are generated from a gaussian distribution with photometric flux and error. The yielded errors of stellar parameters are $\sigma_{T_{\text{eff}}} = 50$ K, $\frac{\sigma_R}{R} = +1.4_{-2.2} \%$ and $\frac{\sigma_L}{L} = +1.36_{-1.37} \%$. This result is considered as typical errors of stellar parameters for all RSGs. Although the T_{eff} we derived exhibit a systematic discrepancy compared to those provided by APOGEE (see Figure 3), the dispersion in their distribution remains at ~ 50 K. Furthermore, the uncertainties in the derived R and L are relatively small, as these parameters were determined through SED convolution. The errors include the observational and model fitting, but do not consider the distance error.

Among these sources, 1950 are observed by APOGEE, whose T_{eff} from the SED fitting is compared with that from the APOGEE high resolution spectrum. As shown in Figure 3, there is an overall consistency between them, which confirms the method. Meanwhile, T_{eff} from the SED fitting is systematically lower than that from APOGEE by 246 K, and the difference has a dispersion of about 46 K. This can be attributed to the difference in stellar model and photometric uncertainty. Furthermore, the atmospheric parameters derived in our study exhibits excellent consistency with the spectroscopic determinations reported by Neugent et al. (2020).

3.2 Identification of RSG Binary

Whether a RSG is a binary is justified by comparing $F'_\nu(\lambda_j)^{\text{mod}}$ with $F'_\nu(\lambda_j)^{\text{obs}}$. $F'_\nu(\lambda_j)^{\text{mod}}$ is the recalculated model flux according to individual T_{eff} from the SED fitting for each RSG, and $F'_\nu(\lambda_j)^{\text{obs}}$ is the recalculated observed flux after correcting interstellar extinction based on the newly calculated λ'_{eff} for T_{eff} . However, the transmissions of some UV filters⁴ have a long tail at long wavelength side, causing the calculated λ_{eff} close to maximum λ of the filter. For these affected filters, we cut off the long tails by removing the minimum 10% of transmission. In addition, the transmission of UVIT filter is unavailable, the mean wavelength of filter is adopted as λ_{eff} ⁵.

By analyzing the L97 model spectra, we find that the larger $\log g$ of RSG, the higher UV model fluxes, but the effect on the NIR wavelengths is small. In addition, the literatures suggest that the $\log g$ of RSG can be up to 0.5 (Levesque 2017). Considering the effects from $\log g$ and T_{eff} , the error of modeled flux is

$$F_\nu^{\text{err}}(\lambda_j)^{\text{mod}} = F_\nu^{\text{max}}(\lambda_j)^{\text{mod}} - F_\nu(\lambda_j)^{\text{mod}}, \quad (6)$$

where $F_\nu^{\text{err}}(\lambda_j)^{\text{mod}}$ is the error of the model flux, $F_\nu^{\text{max}}(\lambda_j)^{\text{mod}}$ is the model fluxes with $\log g = 0.5^6$ and $T_{\text{eff}} = T_{\text{eff}}^{\text{RSG}} + 50$ K. $T_{\text{eff}}^{\text{RSG}}$

⁴ F225W, F170W bands (HST), UVM2, UVW1, UVW2 bands (XMM-OT), UVM2, UVW2, UVW1 bands (Swift/UVOT).

⁵ <https://uvit.iiap.res.in/Instrument/Filters>

⁶ Due to model limitations, $\log g = 0.6$ for $T_{\text{eff}} < 3500$ K.

³ Due to model limitations, $\log g = 0.28$ for $T_{\text{eff}} < 3500$ K.

and $F_\nu(\lambda_j)^{\text{mod}}$ are the T_{eff} and model flux of RSGs from SED fitting (see Section 3.1).

Our binary identification criterion is expressed as

$$F_\nu(\lambda_j)^{\text{obs}} - F_\nu(\lambda_j)^{\text{mod}} > 3F_\nu^{\text{err}}(\lambda_j)^{\text{obs}} + 3F_\nu^{\text{err}}(\lambda_j)^{\text{mod}}, \quad (7)$$

where $F_\nu^{\text{err}}(\lambda_j)^{\text{obs}}$ is the error of observations. The RSG with photometric data at $\lambda_j < 0.4 \mu\text{m}$ that is satisfied with Equation 7 will be identified as a binary. In other words, the star is identified as a binary when the observational flux exceeds the model by three sigma in the UV band. An example of RSG binary SED is shown in Figure 4, where the observed fluxes at $\lambda_{\text{eff}} < 0.4 \mu\text{m}$ are significantly higher than the RSG model spectrum (gray solid line), and it is identified as a binary with a hot companion.

With the criterion described by Equation 7, 1325 and 664 binaries are identified in the LMC and SMC, respectively. The observed binary fraction is then $30.2\% \pm 0.7\%$ (1325/4390) in the LMC and $32.2\% \pm 1\%$ (664/2063) in the SMC and summarized in Table 3. Here, the error in fraction is derived from the binomial distribution. In addition, due to the actual physical separation between the RSG and its putative companion may be remarkably large, the orbital period can reach to $\log P/[\text{d}] \sim 8$ (see discussion in section 4.3). Under conditions of extreme orbital separation, the companion may not only lack significant gravitational interaction with the primary star, but may not be a real binary system. The main results together with the binary fraction of RSGs by other works (see Section 4.4) are listed in Table 3.

3.3 Stellar Parameters of the Companion

Stellar parameters of the companion star for the RSG binaries are further determined by fitting the residual SED after subtracting the RSG model SED from the observed SED. In agreement with the criteria to select hot companion, the wavelengths with $\lambda_{\text{eff}} < 1 \mu\text{m}$ are used to fit the SED of companion. Before fitting the SED of the companion, the *statsmodels* package is used to perform the locally weighted scatterplot smoothing (LOWESS) algorithm to smooth the Gaia/XP, HST/STIS and L97 spectrum. Then, the XP and STIS spectra are used in the process of fitting the companion SED. For unknown reasons, the XP spectra in the range of 600 to 900 nm reduce the goodness of fit, so only the XP spectra from 400 to 600 nm are used. In addition, the PAdova and TRieste Stellar Evolution Code (PARSEC) evolutionary tracks are used to confine the stellar parameter space of companions, which is illustrated in Figure 5. In Figure 5, black circles represent the values of T_{eff} and $\log g$ which are adopted in the SED fitting of the companion. The reduced χ^2 is again calculated by Equation 2.

One example of the companion SED fitting is shown in Figure 6, which shows the best fit of the SED for both the hot companion and RSG (left panel), as well as their positions in the H-R diagram (right panel). The T_{eff} , R , L and $\log g$ derived from the SED fitting are marked as well. Compared to RSGs, the stellar parameters of companions are less accurate because many binaries lack the FUV photometry or with large photometric uncertainty. When fitting the parameters of companions, the varying numbers of UV photometric bands ($\lambda < \sim 0.4 \mu\text{m}$) range from 1 to 8. We present typical T_{eff} uncertainties of companions for T_{eff} ranges corresponding to 3 UV photometric bands (as objects with more than 3 UV bands are fewer). We employed 3,000 MCMC iterations to estimate the uncertainties, which systematically incorporate both T_{eff} of RSGs and photometric measurement errors. The derived median T_{eff} uncertainties for companion stars are 5.8% in the 7,500 - 10,000 K range (73 stars), 5.5%

in the 13,000 - 18,000 K range (31 stars) and 6.2% in the 20,000 - 30,000 K range (10 stars).

Figure 7 shows the H-R diagram of all companion stars and their corresponding RSGs. The gray connecting lines delineate the corresponding associations between individual RSGs and their respective companion stars. The companions are mostly the main-sequence stars with T_{eff} ranging from 6000 K to 30,000 K. The limit at the low end, 6000K, indicates the lower limit of temperature that the UV excess can diagnose. It can be seen that the reduced χ^2 is larger for lower-temperature star because their UV excess is less significant. The higher the temperature, the fewer the number of companions. This agrees with the general distribution. In addition, a few stars are on the horizontal branch, which can be understood by their relatively high temperature. Previous studies suggest that the companions of RSGs are O-,B-,A-type main-sequence stars and most of them are B-type (Bernasconi & Maeder 1996; Neugent et al. 2018, 2019). However, in this work, we find that 56% of the companions (1107/1989) have $T_{\text{eff}} < 7400$ K. The reason is that the effective temperature and radius of a star are coupled, and when the number of available UV bands is small during the SED fitting, the result tends to be at the lower temperature. After eliminating the companions with $T_{\text{eff}} < 7400$ K, the distribution of the remaining companions by temperature is as follows:

- 4.5% (40/882) companions have $T_{\text{eff}} \geq 25,000$ K, corresponding to O-type star.
- 46.3% (408/882) companions have $10,000 \leq T_{\text{eff}} < 25,000$ K, corresponding to B-type star.
- 49.2% (434/882) companions have $7400 \leq T_{\text{eff}} < 10,000$ K, corresponding to A-type star.

Approximately half of the companions belong to the A-type class. These ‘cool’ companions remained undetected in previous surveys. Figure 8 presents the SED fitting diagram of 2MASS J01045611-7215070 with $T_{\text{eff}} = 8250$ K as an illustrative example. While the flux at $\lambda \approx 0.38 \mu\text{m}$ shows no significant excess above the RSG model predictions, a pronounced flux excess becomes evident at $\lambda \leq \sim 0.38 \mu\text{m}$ compared to the RSG model expectations. Neugent et al. (2019) report a sample of 24 RSG+B binaries which are confirmed by spectrum in the LMC and SMC. Our sample has 20 common stars with theirs, and 18 among them are identified as binaries in this work. Such high coincidence (90%) also indicates that the RSG star with hot companion can be identified successfully by the SED fitting method. On the other side, only 11 companions are also identified as B-type star. By checking all the SED fitting diagrams of other stars, it is found that these stars have few or no UV data except the band with $\lambda_{\text{eff}} \approx 0.38 \mu\text{m}$, e.g. SMASH/*u*, SMSS/*u, v*, XMM-OM/*U* and UVOT/*U*. This means that the stellar parameters of companions derived from the SED fitting using only the $\lambda_{\text{eff}} \approx 0.38 \mu\text{m}$ photometric band are not highly reliable and may incline to lower effective temperature. In other words, the RSG binaries can be well identified by the SED fitting based on current UV photometric data, but there is some uncertainty in stellar parameters of the companions, in particular the mid-type stars. The stellar parameters of companions are summarized in Table 2.

4 DISCUSSION

4.1 Identification with HST Spectra

The HST/STIS spectra are searched from MAST to crosscheck the method. It is found that 15⁷ stars have UV spectra consistent with photometric data. As an example shown in Figure 4, the yellow solid line represents the HST/STIS spectrum. All 15 stars are also identified as binaries by the SED fitting method. The stellar parameters of the companions derived from the fitting with and without spectroscopic data are summarized in Table 4. The temperatures of companions derived from two methods are mostly in agreement, which means that our fitting for companions with photometric data is reliable. There are two objects with apparently different T_{eff} , but their $\log L/L_{\odot}$ are roughly the same. This can be understood that the stellar radius is coupled to stellar $\log g$.

4.2 Binary Fraction of RSGs with $\log L/L_{\odot} > 4.0$

The low-luminosity RSGs sample may be contaminated by asymptotic giant branch (AGB) stars (e.g., see Figure 1 in Zhang et al. 2024). In this regard, a purer subsample is obtained by constraining $\log L/L_{\odot} > 4.0$, the same as in, e.g., Neugent et al. (2020). The subsample contains 1532 RSGs in the LMC and 666 RSGs in the SMC, and the binary fraction becomes $26.6\% \pm 1.1\%$ (407/1532) and $26.4\% \pm 1.7\%$ (176/666), respectively. This is 3.6% and 5.8% reduced in comparison with the total sample.

4.3 Detectable Range of Binary Orbital Periods

As previously mentioned, our methodology exhibits insensitivity to the orbital period of binary systems. However, we can effectively estimate the period within the detectable range. We adopted a methodology similar to that employed by Patrick et al. (2022) for estimating the maximum orbital period of binary systems. Their approach utilizes cross-match distance (XMD), which can be regarded as analogous to aperture size, to determine the upper limits of binary orbital periods. The median XMD of our multi-band photometric catalogues is $\sim 0.09'' - 0.4''$ (e.g., demonstrating median XMD values of $0.09''$ between 2MASS and SMASH; $0.4''$ between 2MASS and XMM-OM), yielding an upper limit of $\log P/[d] \sim 8$ for the binary orbital period, or $\sim 30,000$ AU for the orbital separation. Concurrently, the intrinsic physical size constraints of RSGs establish a fundamental lower boundary for binary periods. Previous studies have indicated this minimum period threshold to be $\log P/[d] \sim 2.3$ (Patrick et al. 2020). Consequently, the binary orbital period range derived through our methodology spans approximately $2.3 < \log P/[d] < 8$.

The lower binary fraction of RSGs ($\sim 30\%$) we obtained compared to their progenitors ($\approx 50\% - \approx 70\%$ for OB-type stars) can be reasonably explained through orbital period evolution. The higher binary fraction of OB-type stars is determined through multi-epoch spectroscopy surveys sensitive to orbital periods of $0 \leq \log P/[d] \leq 3$, whereas our detection threshold for RSGs corresponds to a minimum orbital period of $\log P \sim 2.3$ days. Systems with shorter orbital periods than this threshold may have undergone binary merger

events during their evolutionary history, effectively converting potential binary systems into single stars. In addition, our derived binary fraction for RSGs generally exceeds those obtained through RV method. This discrepancy arises because our methodology probes a wider range of orbital periods compared to the more limited period sensitivity range of conventional RV techniques (see Section 1, $3.3 \leq \log P/[d] \leq 4.3$). The extended period coverage in our study enables detection of binary systems that would remain undetected through RV alone. In fact, the fraction of triples among massive stars is considerable (Moe & Di Stefano 2017). The third body significantly influences the evolution of the inner binary (Toonen et al. 2020; Kummer et al. 2023). Combined with a binary fraction of $\sim 50 - 70\%$ within the period range of $0 \leq \log P/[d] \leq 3$, our study suggests that $\sim 1/3$ massive stars hosts a third companion within $\sim 30,000$ AU. In addition, the series of studies by Neugent et al. in section 1 did not explicitly specify their detectable period range. Considering a typical photometric and spectroscopic apertures (e.g. $0.5''$), their detectable period coverage could be similar to ours.

4.4 Comparison with Previous Work on the Fraction of Binary

We compare the binary fractions of RSGs in the LMC (Neugent et al. 2020) and the SMC (Patrick et al. 2022).

Neugent et al. (2020) use a k -nearest neighbors algorithm to calculate the binary fraction of RSG with $\log L/L_{\odot} > 4$ for a sample of 1752 RSGs with likelihood of binarity in the LMC. The binary fraction of RSGs with O- or B-type companions is $13.5^{+7.56}_{-6.67}\%$ (Neugent et al. 2020). By cross-matching with their sample, 1481 stars are common. For these 1481 stars, the binary fraction of Neugent et al. (2020) is 11.55% assuming that stars with likelihood $\geq 50\%$ are binaries, meanwhile the binary fraction of this work is 26.47%, much higher than theirs. Of the 171 stars with likelihood greater than 50%, 133 stars (78%) are also identified by this work. It is worth noting that there are 6 stars⁸ which are binaries with 100% probability by Neugent et al. (2020), but are classified as single stars in this work. However, this does not affect the overall fraction, as the specific discrepancies observed in these 6 stars are detailed in Appendix A. In addition, a comparison of the stellar parameters (T_{eff} , R and L) of 44 common RSGs is shown in Figure 9. The T_{eff} , R and L determined spectroscopically by Neugent et al. (2020) are in general agreement with those from this work, with the μ and σ of residuals shown by insets in Figure 9.

Patrick et al. (2022) report a binary fraction of $15.7 \pm 1.5\%$ for RSGs in the SMC by the detection in the UVIT/F172M band because single RSGs are non-detectable at this wavelength. In their sample of 862 RSG candidates in the SMC, 560 RSGs are located in the footprint of the UVIT survey. They find 88 stars detected in the F172M band and attribute to the presence of hot companions. By cross-matching with the 862 RSG candidates of Patrick et al. (2022), 654 RSGs are common. The binary fraction of this sample is 28.75% in this work, which is about twice of 15.7%. This can be understood because the F172M filter is sensitive only to very hot stars as the effective wavelength corresponds to a Wien temperature of $\sim 17,000\text{K}$. For the 88 stars detected in UVIT/F172M, 84 of them are included in this work. Except one has the reduced χ^2 above the 95% confidence level, the other 83 stars are all binaries identified by this work. This implies that our method can identify more than 95%

⁷ 2MASS J00513280-7205493, J00522647-7245159, J00532362-7247013, J00533967-7232089, J00534451-7233192, J00580864-7219270, J01010366-7202588, J01023794-7235547, J01024076-7217173, J01024208-7237294, J01031094-7218327, J01031855-7206461, J01052742-7217044, J01081478-7246411 and J01101248-7237310.

⁸ 2MASS J04543854-6911170, J04595731-6748133, J05170897-6932211, J05284548-6858022, J05292757-6908502 and J05414402-6912027.

binaries with UV excess. It also means that a small fraction is missed during our removal of poor SED fitting caused by the UV excess.

4.5 UV Excess in the Color-color Diagrams

Theoretically, RSG with hot companion should have smaller $(UV - NIR)_0$ than single RSG because of the higher UV emission by the companion. Then, the RSG binaries should appear below the main single branch in the $(UV - NIR)_0$ vs. $(J - K_S)_0$ diagram since the NIR color is determined only by RSG. Figure 10 shows the distribution in the $(u - J)_0$ vs. $(J - K_S)_0$ diagram for the RSG stars in the LMC (left) and SMC (right). The red solid dots and the gray circles denote the RSG binaries and singles respectively identified in this work. Clearly, there is a concentrated narrow band at the upper side, which is consistent with two previous results displayed, i.e. the light-blue shaded area for the RSG single stars calculated by the PARSEC model (Bressan et al. 2012), and the blue dashed line for the RSG sample of Wang & Chen (2023). It can be seen that there is a systematic shift between them, with the result of Wang & Chen (2023) closer to the main population of the sample in this work. The reason for the difference may be the presence of chromospheric activity of RSGs, which leads to smaller UV fluxes predicted by the PARSEC model (Carpenter & Rau 2019). Meanwhile, there are some binaries in the single star sequence. Though these binaries have a hotter companion, the companion is not so hot to augment the flux in the SMASH u band significantly. In addition, there are a few stars beyond the upper bound of the PARSEC model, which may be caused by incorrect photometry in the SMASH u band.

As expected, the stars below the main branch are mostly binaries. For the stars detected in the SMASH u band, the binary fraction is 31.57% in the LMC and 32.54% in the SMC. By replacing the SMASH u band by the UVW1 band, a similar color-color diagram is presented in Figure 11 as the $(UVW1 - J)_0$ vs. $(J - K_S)_0$ diagram. Then, the binary fraction is up to 88.38% for the LMC and 70.8% for the SMC in the RSG sample detected in the UVW1 band. The great increase in the UVW1 band is understandable since the effective wavelength is shorter for the UVW1 with $\lambda_{\text{eff}} \sim 0.29\mu\text{m}$ band than the SMASH u band with $\lambda_{\text{eff}} \sim 0.38\mu\text{m}$. The small shift to UV band greatly increases the detection efficiency of hot companions for RSGs, which may guide to the future observational preference.

4.6 Additional Evidences and Limitations

In addition to the SED fitting method, the RSG binaries are also searched by the light curve (LC) and RV methods. It is found that 13 LCs have significant eclipsing characteristic after cross-matching with the eclipsing binary catalog of Faccioli et al. (2007) and Pawlak et al. (2016). These stars are all identified as binaries in this work.

For the RV method, the APOGEE provides an opportunity for its high spectral resolution and multiple visits to one object. The epoch RV data are taken from APOGEE/DR17. The method is similar to previous studies to calculate the RV variation (Sana et al. 2013; Dunstall et al. 2015; Patrick et al. 2019; Dorda & Patrick 2021). The stars with significant variation are firstly selected by:

$$\frac{|v_i - v_j|}{\sqrt{\sigma_i^2 + \sigma_j^2}} > 3, \quad (8)$$

where v_i and v_j are any two epochs RVs of the source, and σ_i and σ_j are the corresponding uncertainties. Moreover, the $|\Delta V_{\text{max}}|$ is defined as the maximum difference of RV, and the binary criterion of $|\Delta V_{\text{max}}| > 11 \text{ km s}^{-1}$ is adopted as suggested by Dorda & Patrick

(2021). This yields 10 RSG binaries in our sample. Among the 10 RSG binaries, two are identified by the UV excess in this work. In addition, Gaia DR3 provides $|\Delta V_{\text{max}}|$ of RV as well, but no epoch RV. Due to lack of epoch RV data, only the criterion of $|\Delta V_{\text{max}}| > 11 \text{ km s}^{-1}$ is adopted, which results in 355 binary candidates. Among the 355 binary candidates, 92 are identified by the UV excess in this work, a much larger number than the APOGEE result. The reason may come from two sides. One is that the Gaia criterion is not so strict so that the candidates are contaminated significantly by single stars. The other is that our estimation can only find the binaries with hot companions while the RV method is not limited by this factor. The binaries identified by the LC and RV methods are summarized in Table 5.

In this work, our method relies on the UV observations, depending on detection of the excess UV fluxes to identify the presence of hot companion. The RSG binaries with cool companions cannot be identified in this way because the fluxes of cool companion will be mixed with RSGs as evidenced by the lower limit of $T_{\text{eff}} = 6000 \text{ K}$ of the companion. In addition, some stars may be absent of UV photometry or the UV fluxes of companion may be eclipsed by RSG. Therefore, our results should be taken as the lower limit of RSG binary fraction.

4.7 Potential Contamination of Binary Fraction

4.7.1 UV excess by Circumstellar Dust

UV excess can be caused by sufficient circumstellar dust of RSG, which is indicated by the linear relation of the NUV excess with dust production rate \dot{M}_d and extra extinction (Massey et al. 2005). The average \dot{M}_d are on the order of $10^{-10} \text{ M}_{\odot} \text{ yr}^{-1}$ and $10^{-11} \text{ M}_{\odot} \text{ yr}^{-1}$ in the LMC and SMC, respectively (Riebel et al. 2012; Boyer et al. 2012; Srinivasan et al. 2016; Wen et al. 2024). With such low dust production rate due to the low metallicity of MCs, the NUV excess from circumstellar dust scattering is expected to be negligible. Thus the circumstellar dust scattering can not account for the observed UV excess.

In addition, the UV excess if caused by circumstellar dust should correlate with the IR excess. However, as shown in Figure 12, there is no correlation between the UV excess represented by the modeled magnitude minus the observed for SMASH u and the IR excess represented by the modeled magnitude minus observed for WISE W2. The distribution of IR excess is concentrated for the most stars, except two stars⁹ pointed by the black arrows. Therefore, the effect of circumstellar dust on binary fraction is small in this work.

4.7.2 Contamination Probability from Line of Sight

As mentioned in the work of Neugent et al. (2020) and Neugent (2021), a possible contaminant is line of sight pairings. This means that the UV excess of RSGs do not come from real hot companion, but from foreground or background stars of the MCs. They find a contamination rate of $1.9\% \pm 2.0\%$ for OB companions. To calculate the contamination rate in this work, a similar method is applied as described in Neugent et al. (2020). Firstly, the OBA stars in the studied area are selected from Gaia DR3 by the intrinsic color $(G_{\text{BP}} - G_{\text{RP}})_0$ and T_{eff} . We set $T_{\text{eff}} = 7400 \text{ K}$ as the lower limit of A type stars, and the corresponding $(G_{\text{BP}} - G_{\text{RP}})_0$ is calculated as = 0.44 and 0.38 in the LMC and SMC, respectively (Zhao et al. 2020; Cao et al. 2023).

⁹ 2MASS J05482065-7346202 and 04490798-6907191.

An average $E(B - V) = 0.13$ and 0.09 are adopted (Massey et al. 2007a) and converted to $E(G_{BP} - G_{RP})$ with the extinction law by Wang & Chen (2019, 2023). Then, for each RSG binary determined in Section 3.2, the locations of all OBA stars are searched within a $5'$ radius of the RSG binary. Finally, we randomly move the binary to another position within $5'$. If the new position is within $1''$ of any OBA stars, it means a line of sight pairing. An MCMC code¹⁰ is run 10,000 times for each RSG binary. A $4.33\% \pm 1.84\%$ contamination rate is found in this work. This means that the contamination rate is $4.33\% \pm 1.84\%$ for the whole sample, while $1.9\% \pm 2.0\%$ for the sample with $\log L/L_{\odot} > 4.0$.

5 SUMMARY

In this work, we calculate the binary fraction of RSGs in the LMC and SMC by the SED fitting method in the sample of 4695 (LMC) and 2097 (SMC) RSGs. After fitting the SEDs of RSGs, the RSG binaries are identified by comparing the observed flux with the modeled flux of the RSGs in the UV bands. It is found that the binary fraction of RSGs is $30.2\% \pm 0.7\%$ in the LMC and $32.2\% \pm 1\%$ in the SMC for the whole sample, while it is $26.6\% \pm 1.1\%$ in the LMC and $26.4\% \pm 1.7\%$ in the SMC for sample of RSGs with $\log L/L_{\odot} > 4.0$. The detectable period range associated with our methodology spans $\sim 2.3 < \log P/[d] < \sim 8$. In addition, the possible contamination rate by chance sight line pairing is $4.33\% \pm 1.84\%$ for the whole sample and $1.9\% \pm 2.0\%$ for the sample with $\log L/L_{\odot} > 4.0$. Due to the limitations of method and data, this result should be the lower limit of binary fraction in the RSGs. In the process of the SED fitting, the stellar parameters, i.e. the T_{eff} , R and L of the RSGs, and the T_{eff} , R , L and $\log g$ of the companions are derived. Among the binary RSGs identified by the SED fitting, 15 are supported by fitting the HST/STIS spectra. In addition to the SED fitting method, the LC and RV methods are used to confirm our identification of binaries for a small part of the sample.

ACKNOWLEDGEMENTS

We are grateful to the anonymous referee for his very helpful comments and suggestions to improve this paper. We are also grateful to Drs. Xiaodian Chen, Jun Li, Yi Ren and Ming Yang for their helpful discussion and suggestion. This work is supported by the NSFC project 12133002 and 12373028, National Key R&D Program of China No. 2019YFA0405500, and CMS-CSST-2021-A09. S.W. acknowledges the support from the Youth Innovation Promotion Association of the CAS (grant No. 2023065). The numerical computations were conducted on the Qilu Normal University High Performance Computing, Jinan Key Laboratory of Astronomical Data. This work has made use of the data from SMASH, 2MASS, Gaia, XMM-OM, *Swift*/UVOT, UVIT, HST, GALEX, SMSS, SPITZER, WISE surveys.

DATA AVAILABILITY

The data underlying this article are available in the article and in its online supplementary material. The data underlying this article will be shared on reasonable request to the corresponding author.

¹⁰ <https://github.com/KNeugent/LineOfSightBinaries>

REFERENCES

- Abdurro'uf et al., 2022, *ApJS*, 259, 35
 Bernasconi P. A., Maeder A., 1996, *A&A*, 307, 829
 Bianchi L., Shiao B., Thilker D., 2017, *ApJS*, 230, 24
 Boyer M. L., et al., 2012, *ApJ*, 748, 40
 Bressan A., Marigo P., Girardi L., Salasnich B., Dal Cero C., Rubele S., Nanni A., 2012, *MNRAS*, 427, 127
 Cao Z., Jiang B., Zhao H., Sun M., 2023, *ApJ*, 945, 132
 Carpenter K. G., Rau G., 2019, in Kerschbaum F., Groenewegen M., Olofsson H., eds, Vol. 343, *Why Galaxies Care About AGB Stars: A Continuing Challenge through Cosmic Time*. pp 365–367, doi:10.1017/S1743921318005872
 Carrasco J. M., et al., 2021, *A&A*, 652, A86
 Catchpole R. M., Feast M. W., 1981, *Monthly Notices of the Royal Astronomical Society*, 197, 385
 Crandall S., Ratra B., 2015, *ApJ*, 815, 87
 Cutri R. M., et al., 2003, *VizieR Online Data Catalog*, p. II/246
 Cutri R. M., et al., 2021, *VizieR Online Data Catalog*, p. II/328
 Davies B., et al., 2013, *ApJ*, 767, 3
 Devaraj A., Joseph P., Stalin C. S., Tandon S. N., Ghosh S. K., 2023, *ApJ*, 946, 65
 Dorda R., Patrick L. R., 2021, *MNRAS*, 502, 4890
 Dunstall P. R., et al., 2015, *A&A*, 580, A93
 Eldridge J. J., Xiao L., Stanway E. R., Rodrigues N., Guo N. Y., 2018, *Publ. Astron. Soc. Australia*, 35, e049
 Faccioli L., Alcock C., Cook K., Prochter G. E., Protopapas P., Syphers D., 2007, *AJ*, 134, 1963
 Feast M. W., Catchpole R. M., Carter B. S., Roberts G., 1980, *Monthly Notices of the Royal Astronomical Society*, 193, 377
 Gaia Collaboration et al., 2021, *A&A*, 649, A1
 Gaia Collaboration et al., 2023, *A&A*, 674, A1
 García B., Mermilliod J. C., 2001, *A&A*, 368, 122
 Gehrels N., 2004, in Fenimore E., Galassi M., eds, *American Institute of Physics Conference Series Vol. 727, Gamma-Ray Bursts: 30 Years of Discovery*. pp 637–641, doi:10.1063/1.1810924
 Gies D. R., 2008, in Beuther H., Linz H., Henning T., eds, *Astronomical Society of the Pacific Conference Series Vol. 387, Massive Star Formation: Observations Confront Theory*. p. 93
 González-Fernández C., Dorda R., Negueruela I., Marco A., 2015, *A&A*, 578, A3
 Groh J. H., Meynet G., Georgy C., Ekström S., 2013, *A&A*, 558, A131
 Gunn J. E., et al., 2006, *AJ*, 131, 2332
 Hutchings J. B., 2014, *Ap&SS*, 354, 143
 Jansen F., et al., 2001, *A&A*, 365, L1
 Kobulnicky H. A., et al., 2014, *ApJS*, 213, 34
 Kumar A., et al., 2012, in Takahashi T., Murray S. S., den Herder J.-W. A., eds, *Society of Photo-Optical Instrumentation Engineers (SPIE) Conference Series Vol. 8443, Space Telescopes and Instrumentation 2012: Ultraviolet to Gamma Ray*. p. 84431N (arXiv:1208.4670), doi:10.1117/12.924507
 Kummer F., Toonen S., de Koter A., 2023, *A&A*, 678, A60
 Lejeune T., Cuisinier F., Buser R., 1997, *A&AS*, 125, 229
 Levesque E. M., 2017, *Astrophysics of Red Supergiants*, doi:10.1088/978-0-7503-1329-2
 Levesque E. M., Massey P., Olsen K. A. G., Plez B., Josselin E., Maeder A., Meynet G., 2005, *ApJ*, 628, 973
 Majewski S. R., et al., 2017, *AJ*, 154, 94
 Mason B. D., Gies D. R., Hartkopf W. I., Bagnuolo William G. J., ten Brummelaar T., McAlister H. A., 1998, *AJ*, 115, 821
 Mason K. O., et al., 2001, *A&A*, 365, L36
 Massey P., 2002, *The Astrophysical Journal Supplement Series*, 141, 81
 Massey P., Evans K. A., 2016, *ApJ*, 826, 224
 Massey P., Olsen K. A. G., 2003, *The Astronomical Journal*, 126, 2867
 Massey P., Plez B., Levesque E. M., Olsen K. A. G., Clayton G. C., Josselin E., 2005, *ApJ*, 634, 1286
 Massey P., Olsen K. A. G., Hodge P. W., Jacoby G. H., McNeill R. T., Smith R. C., Strong S. B., 2007a, *AJ*, 133, 2393
 Massey P., Levesque E. M., Olsen K. A. G., Plez B., Skiff B. A., 2007b, *ApJ*,

- 660, 301
- Massey P., Levesque E. M., Plez B., Olsen K. A. G., 2008, in Bresolin F., Crowther P. A., Puls J., eds, Vol. 250, *Massive Stars as Cosmic Engines*, pp 97–110 ([arXiv:0801.1806](https://arxiv.org/abs/0801.1806)), doi:10.1017/S1743921308020383
- Massey P., Neugent K. F., Dorn-Wallenstein T. Z., Eldridge J. J., Stanway E. R., Levesque E. M., 2021, *The Astrophysical Journal*, 922, 177
- Medallion S., Rickman E., Brown J. e. a., 2023, *STIS Instrument Handbook*
- Moe M., Di Stefano R., 2017, *ApJS*, 230, 15
- Montegriffo P., et al., 2023, *A&A*, 674, A3
- Morrissey P., et al., 2005, *ApJ*, 619, L7
- Morrissey P., et al., 2007, *ApJS*, 173, 682
- Neugent K. F., 2021, *ApJ*, 908, 87
- Neugent K. F., Massey P., Skiff B., Meynet G., 2012, *The Astrophysical Journal*, 749, 177
- Neugent K. F., Levesque E. M., Massey P., 2018, *AJ*, 156, 225
- Neugent K. F., Levesque E. M., Massey P., Morrell N. I., 2019, *ApJ*, 875, 124
- Neugent K. F., Levesque E. M., Massey P., Morrell N. I., Drout M. R., 2020, *ApJ*, 900, 118
- Nidever D. L., et al., 2017, *AJ*, 154, 199
- Nidever D. L., et al., 2021, *AJ*, 161, 74
- Onken C. A., et al., 2019, *Publ. Astron. Soc. Australia*, 36, e033
- Page M. J., et al., 2012, *MNRAS*, 426, 903
- Patrick L. R., et al., 2019, *A&A*, 624, A129
- Patrick L. R., et al., 2020, *A&A*, 635, A29
- Patrick L. R., Thilker D., Lennon D. J., Bianchi L., Schootemeijer A., Dorda R., Langer N., Negueruela I., 2022, *MNRAS*, 513, 5847
- Pawlak M., et al., 2016, *Acta Astron.*, 66, 421
- Pierce M. J., Jurcevic J. S., Crabtree D., 2000, *Monthly Notices of the Royal Astronomical Society*, 313, 271
- Piridi S., Kumar R., Pandey D., Pradhan A. C., 2024, *ApJS*, 275, 34
- Ren Y., Jiang B., Yang M., Wang T., Ren T., 2021, *ApJ*, 923, 232
- Riebel D., Srinivasan S., Sargent B., Meixner M., 2012, *ApJ*, 753, 71
- Roming P. W. A., et al., 2005, *Space Sci. Rev.*, 120, 95
- Ruz-Mieres D., zuzannakr 2023, *gaia-dpci/GaiaXPY: GaiaXPY v2.1.0*, doi:10.5281/zenodo.8239995, <https://doi.org/10.5281/zenodo.8239995>
- Sana H., et al., 2012, *Science*, 337, 444
- Sana H., et al., 2013, *A&A*, 550, A107
- Sana H., et al., 2014, *ApJS*, 215, 15
- Shenar T., 2024, *arXiv e-prints*, p. arXiv:2410.16114
- Shenar T., et al., 2022, *A&A*, 665, A148
- Singh K. P., et al., 2014, in Takahashi T., den Herder J.-W. A., Bautz M., eds, *Society of Photo-Optical Instrumentation Engineers (SPIE) Conference Series Vol. 9144, Space Telescopes and Instrumentation 2014: Ultraviolet to Gamma Ray*, p. 91441S, doi:10.1117/12.2062667
- Skowron D. M., et al., 2021, *ApJS*, 252, 23
- Skrutskie M. F., et al., 2006, *AJ*, 131, 1163
- Spitzer Science Center (SSC) Infrared Science Archive (IRSA) 2021, *VizieR Online Data Catalog*, p. II/368
- Srinivasan S., Boyer M. L., Kemper F., Meixner M., Sargent B. A., Riebel D., 2016, *MNRAS*, 457, 2814
- Toonen S., Portegies Zwart S., Hamers A. S., Bandopadhyay D., 2020, *A&A*, 640, A16
- Wang S., Chen X., 2019, *ApJ*, 877, 116
- Wang S., Chen X., 2023, *ApJ*, 946, 43
- Wen J., Gao J., Yang M., Chen B., Ren Y., Wang T., Jiang B., 2024, *AJ*, 167, 51
- Werner M. W., et al., 2004, *ApJS*, 154, 1
- Whitmore B. C., et al., 2016, *AJ*, 151, 134
- Wilson J. C., et al., 2019, *PASP*, 131, 055001
- Wittkowski M., Hauschildt P. H., Arroyo-Torres B., Marcaide J. M., 2012, *A&A*, 540, L12
- Wolf C., et al., 2018, *Publ. Astron. Soc. Australia*, 35, e010
- Wood P. R., Bessell M. S., Fox M. W., 1983, *ApJ*, 272, 99
- Woolley S. E., Heger A., 2006, *ApJ*, 637, 914
- Wright E. L., et al., 2010, *AJ*, 140, 1868
- Yang M., Jiang B. W., 2011, *The Astrophysical Journal*, 727, 53
- Yang M., Jiang B. W., 2012, *The Astrophysical Journal*, 754, 35
- Yang M., et al., 2020, *A&A*, 639, A116
- Yang M., et al., 2021, *A&A*, 646, A141
- Yang M., et al., 2024, *ApJ*, 965, 106
- Yershov V. N., 2014, *Ap&SS*, 354, 97
- Zapartas E., et al., 2019, *A&A*, 631, A5
- Zaritsky D., Harris J., Thompson I. B., Grebel E. K., Massey P., 2002, *AJ*, 123, 855
- Zaritsky D., Harris J., Thompson I. B., Grebel E. K., 2004, *AJ*, 128, 1606
- Zhang Z., Ren Y., Jiang B., Soszyński I., Jayasinghe T., 2024, *ApJ*, 969, 81
- Zhao H., Jiang B., Li J., Chen B., Yu B., Wang Y., 2020, *ApJ*, 891, 137
- de Grijs R., Wicker J. E., Bono G., 2014, *AJ*, 147, 122

APPENDIX A: STELLAR CLASSIFICATION COMPARISON OF SIX STARS

Of these, 2MASS J04543854-6911170 and J05292757-6908502 are identified as binaries by direct spectroscopy by Neugent et al. (2020), and should be reliable binary. In such rare conflict, it may be due to that the photometric epoch is not at the right orbital phase to expose the UV excess. For the other four stars, the Magellanic Clouds Photometric Survey (MCPS, Zaritsky et al. 2002, 2004) *U* band photometric data used in Neugent et al. (2020) is discrepant with the SMASH *u* band data used in this work. In detail, the difference between the two observations, SMASH *u* – MCPS *U*, is 3.49, 2.76, 2.37 and 3.29 mag for 2MASS J04595731-6748133, J05170897-6932211, J05284548-6858022 and J05414402-6912027, while the systematic difference between the two bands is $\mu = 0.81$ with $\sigma = 0.16$ due to that MCPS uses the Vega system and SMASH uses the AB system. Because MCPS uses a 1-m telescope while SMASH uses a 4-m telescope, the photometric quality of SMASH is better, especially in dense star fields. The brighter photometric data may have been responsible for the identification of the above four stars as binaries by the work of Neugent et al. (2020). In addition, the MCPS *U* photometry covers only 76.5% of our sample, whereas the SMASH *u* photometry covers 92.24% of our sample. As shown in Figure A1, the six stars should be single stars based on the SED fitting method, and they all show significant infrared excess indicating the existence of circumstellar dust.

This paper has been typeset from a $\text{\TeX}/\text{\LaTeX}$ file prepared by the author.

Table 1. The information of all filters used for constructing SED.

Facility/Instrument	Filter(effective wavelength, unit in μm)
HST	F170W(0.19), F225W(0.24), F275W(0.27), F280N(0.28), F300W(0.30), F336W(0.33), F343N(0.34), F373N(0.37)
GALEX	FUV(0.15), NUV(0.23)
UVIT	F154W(0.15), F169M(0.16), F172M(0.17), N219M(0.22), N245M(0.24), N263M(0.26), N279N(0.28)
<i>Swift</i> /UVOT	UVW2(0.21), UVM2(0.22), UVW1(0.28), <i>U</i> (0.35), <i>B</i> (0.44), <i>V</i> (0.55)
XMM-OM	UVW2(0.20), UVM2(0.23), UVW1(0.29), <i>U</i> (0.35), <i>B</i> (0.43), <i>V</i> (0.54)
SMASH	<i>u</i> (0.36), <i>g</i> (0.47)
SMSS	<i>u</i> (0.35), <i>v</i> (0.39), <i>g</i> (0.50), <i>r</i> (0.61), <i>i</i> (0.77), <i>z</i> (0.91)
APASS	Johnson: <i>B</i> (0.43), <i>V</i> (0.54); SDSS: <i>g'</i> (0.46), <i>r'</i> (0.61), <i>i'</i> (0.74)
Gaia	<i>G</i> _{BP} (0.50), <i>G</i> _{RP} (0.76)
2MASS	<i>J</i> (1.24), <i>H</i> (1.66), <i>K</i> _S (2.16)
SPITZER	IRAC: [3.6] (3.51), [4.5] (4.44), [5.8] (5.63), [8.0] (7.59); MIPS: [24] (23.21)
WISE	W1(3.35), W2(4.60), W3(11.56), W4(22.09)

^a The effective wavelength for Vega is taken from SVO Filter Profile Service¹¹.

Table 2. Stellar parameters of RSGs in the Magellanic Clouds. A full version of this table is available as supplementary material.

2MASS	RSG			Companion			Type ^d	
	T_{eff}^a	R/R_{\odot}^b	$\log L/L_{\odot}^c$	T_{eff}	R/R_{\odot}	$\log L/L_{\odot}$		$\log g$
LMC								
04160129-7136083	3750	289	4.17					S
04191178-6544192	3800	126	3.47					S
...
04182834-7741567	4150	143	3.74	7500	11	2.53	0.5	B
04262486-6618046	4250	122	3.64	8500	10	2.64	4.5	B
SMC								
00082691-7216537	4200	304	4.42					S
00105622-7520144	4250	108	3.54					S
...
01411596-7333447	4200	139	3.74	10500	8	2.86	2.0	B
01421678-7316371	3700	431	4.5	6000	29	2.98	2.5	B

^a Typical uncertainty 50 K.

^b Typical relative uncertainty $^{+1.4}_{-2.2}$ %.

^c Typical relative uncertainty $^{+1.36}_{-1.37}$ %.

^d S = single star, B = binary system.

The unit of T_{eff} is K, R is R_{\odot} and L is L_{\odot} .

Table 3. Binary fraction of RSGs.

Region	Fraction	Method	Reference
LMC	30.2% / 26.6% ^a	<i>SED fitting</i>	<i>This work</i>
LMC	19.5 $^{+7.6}_{-6.7}$ %	Machine learning based on spectrum	Neugent et al. (2020)
LMC 30 Doradus	Up limit 30%	RV	Patrick et al. (2019)
LMC	14 \pm 5 %	RV	Dorda & Patrick (2021)
SMC	32.2% / 26.4% ^b	<i>SED fitting</i>	<i>This work</i>
SMC	15.7 \pm 1.5 %	Detected FUV flux	Patrick et al. (2022)
SMC NGC 330	30 \pm 10 %	RV	Patrick et al. (2020)
SMC	15 \pm 4 %	RV	Dorda & Patrick (2021)
M31	Internal 41.2 $^{+12.0}_{-7.3}$ External 15.9 $^{+12.4}_{-1.9}$	Machine learning based on spectrum	Neugent (2021)
M33	33.5 $^{+8.6}_{-5.0}$ %	Machine learning based on spectrum	Neugent (2021)

^a The former is the fraction for the whole sample, and the latter is for the subsample with $\log L/L_{\odot} > 4.0$.

^b The same as 'a'.

Table 4. Stellar parameters of the companions derived from photometry and spectrum.

2MASS	T_{eff}		R/R_{\odot}		$\log L/L_{\odot}$	
	by photometry	by spectrum	by photometry	by spectrum	by photometry	by spectrum
00513280-7205493	16000	18000	14	12	4.08	4.13
00522647-7245159	17000	20000	14	12	4.2	4.3
00532362-7247013	17000	21000	9	6	3.81	3.84
00533967-7232089	14000	15000	13	12	3.75	3.81
00534451-7233192	15000	15000	13	13	3.89	3.9
00580864-7219270	14000	13000	4	5	2.8	2.76
01010366-7202588	9500	16000	19	6	3.42	3.33
01023794-7235547	15000	19000	13	9	3.9	4.0
01024076-7217173	14000	19000	12	7	3.68	3.72
01024208-7237294	10500	12500	9	7	2.9	3.06
01031094-7218327	11500	15000	14	8	3.48	3.52
01031855-7206461	11000	17000	19	11	3.68	3.98
01052742-7217044	19000	21000	8	7	3.91	3.92
01081478-7246411	10500	8250	8	21	2.79	3.27
01101248-7237310	14000	14000	6	7	3.13	3.17

The unit of T_{eff} is K, R is R_{\odot} and L is L_{\odot} .

Table 5. RSG binaries identified by the LC and RV methods. A full version of this table is available as supplementary material.

2MASS	method ^{a, b}	$ \Delta V_{\text{max}} ^c$	$ \Delta V_{\text{max}} ^d$	This work ^e
LMC				
04444215-6924427	LC[a]			B
04455518-6915438	LC[a]			B
...
04355829-7142264	RV	16.7		S
06000792-6809109	RV		13.1	S
SMC				
01000495-7246106	LC[a]			B
01002813-7303072	LC[a]			B
...
01303395-7318417	RV		16.7	S
01330779-7402383	RV		12.0	S

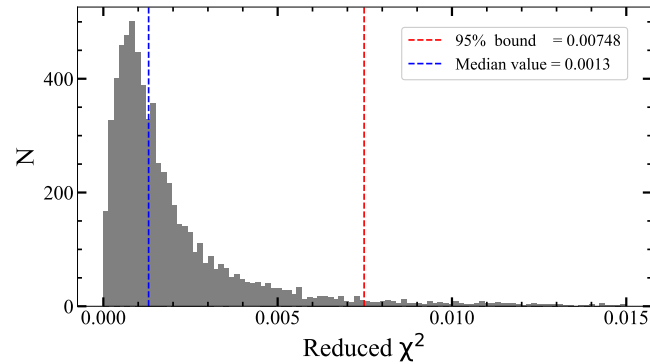
^a From Pawlak et al. (2016).

^b From Faccioli et al. (2007).

^c $|\Delta V_{\text{max}}|$ from APOGEE DR17.

^d $|\Delta V_{\text{max}}|$ from Gaia DR3.

^e S = single star, B = binary system, null value = star with χ^2 above the 95% confidence level.


Figure 1. The reduced χ^2 distribution derived from the SED fitting of RSGs. The red dashed line and the blue dashed line represent the 95% confidence interval and the median value of our sample, respectively.

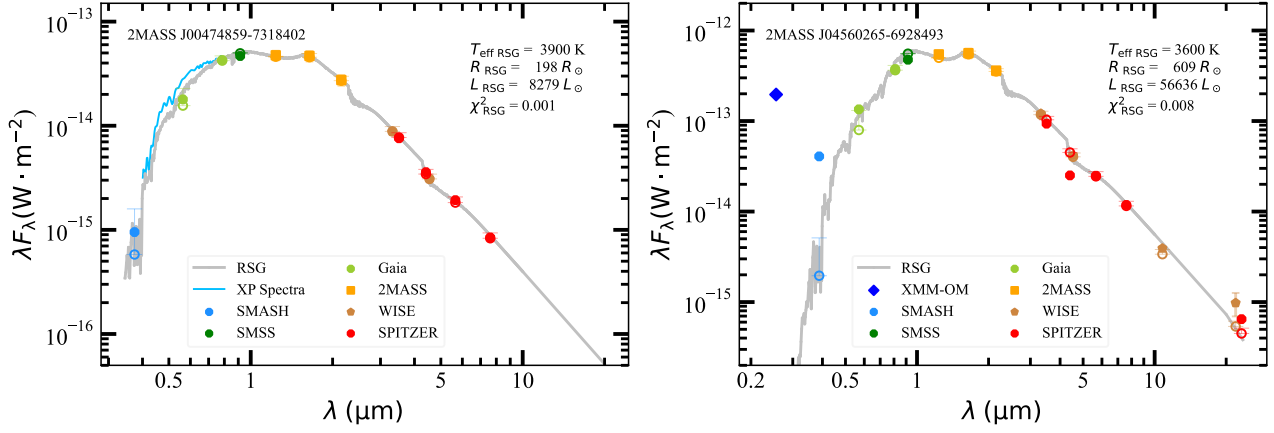


Figure 2. The examples of the RSG SED fitting for 2MASS J00474859-7318402 and J04560265-6928493. The left panel shows a single RSG SED with a reduced χ^2 around the median value, and the right panel shows a binary SED with a reduced χ^2 greater than the 95% confidence value. The gray solid line represents the L97 model spectrum, and the blue solid line represents the XP spectra. The solid and hollow markers with 3σ error bars show the photometry and model data. The coordinate is marked on the upper left, and T_{eff} , R , L and χ^2 are displayed on the upper right. The symbol conversions are followed in the following figures.

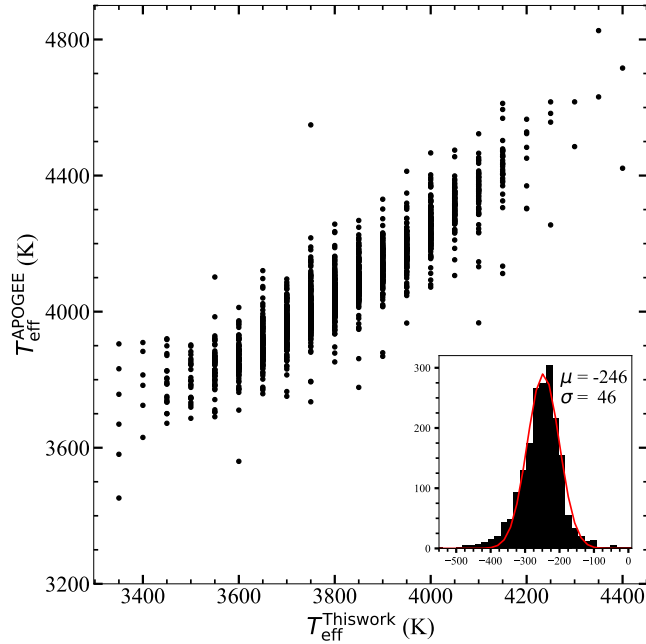


Figure 3. A comparison of T_{eff} from APOGEE and from the SED fitting. The μ and σ of residual are presented in the inset.

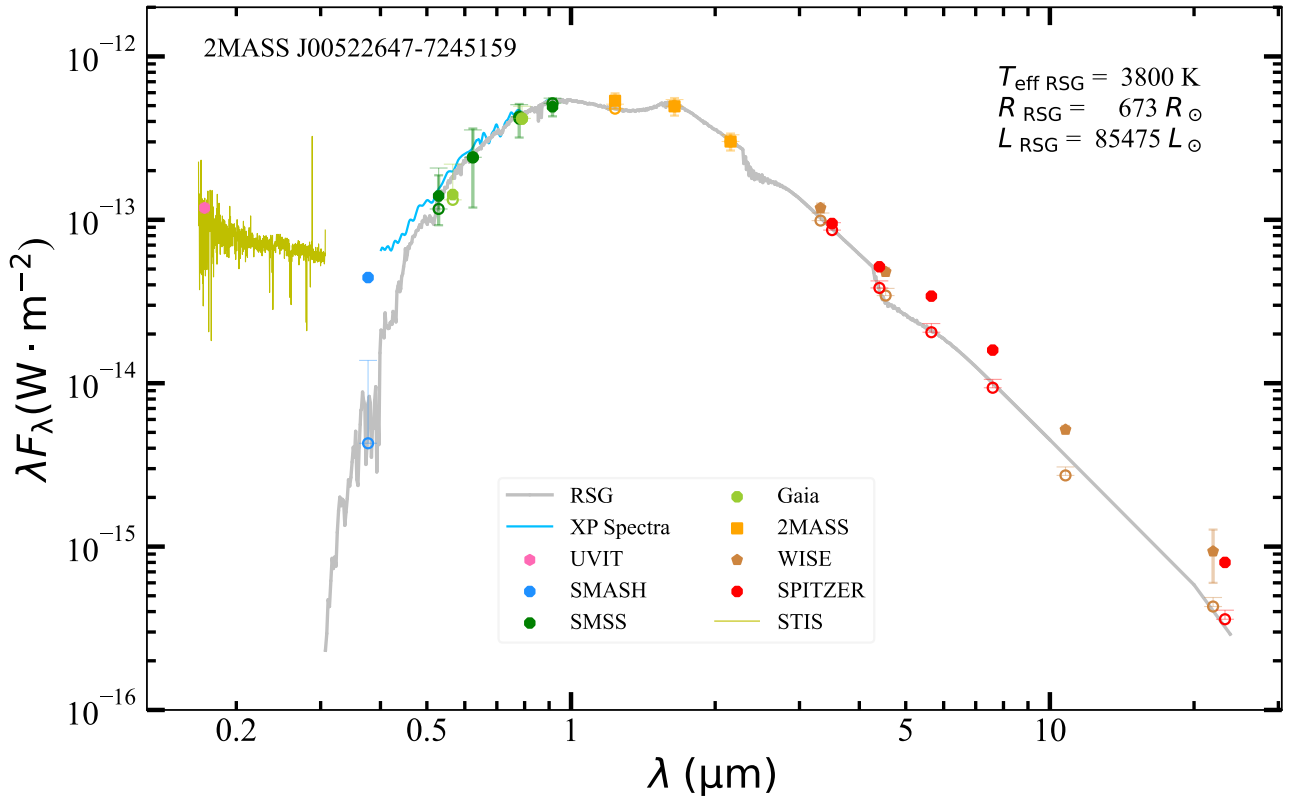


Figure 4. An example of the SED fitting to the RSG component of a binary candidate, 2MASS J00522647-7245159.

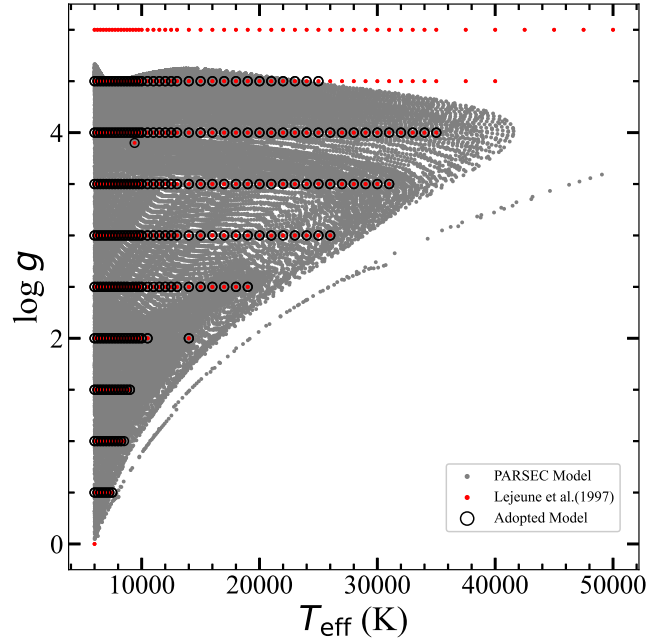


Figure 5. The parameters space (T_{eff} vs. $\log g$) for fitting the companion star. The red and gray solid dots represent the L97 and PARSEC model, respectively. The black circles denote the adopted stellar parameters in this work.

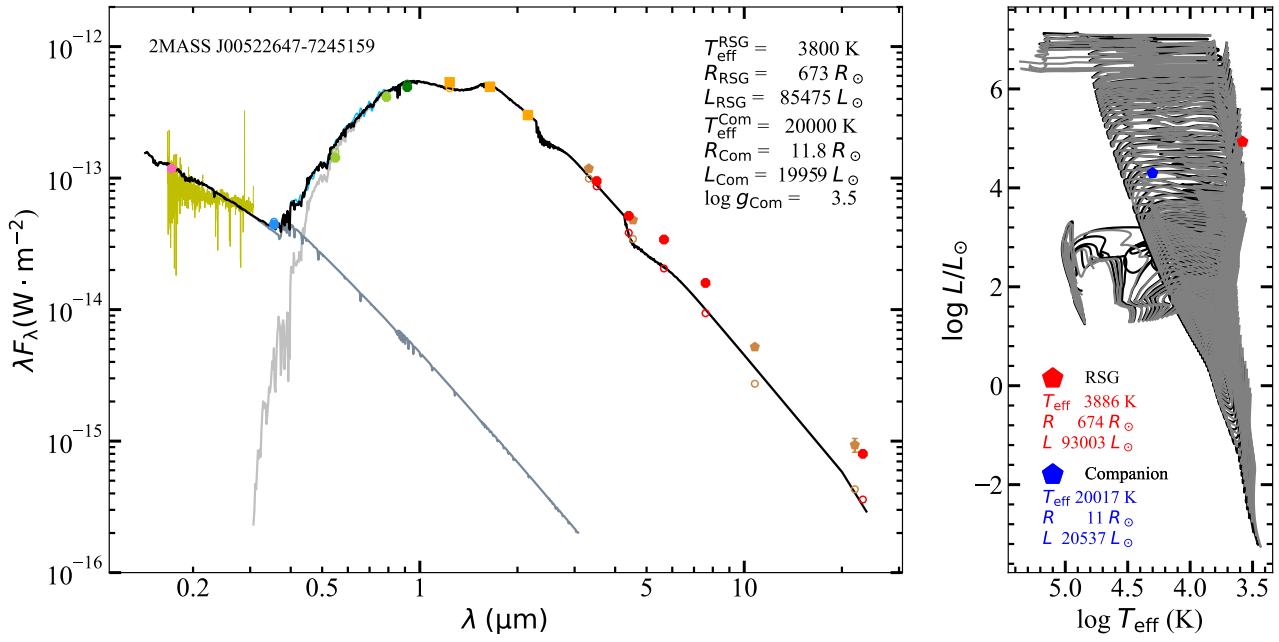


Figure 6. An example of the SED fitting for the companion star. The left panel is similar to Figure 4. The right panel shows the locations of RSG (red) and companion (blue) in the H-R diagram. The black and gray lines represent different metallicity of the PARSEC evolutionary tracks, at $Z = 0.004$ and 0.006 for LMC, $Z = 0.001$ and 0.002 for SMC (Bressan et al. 2012).

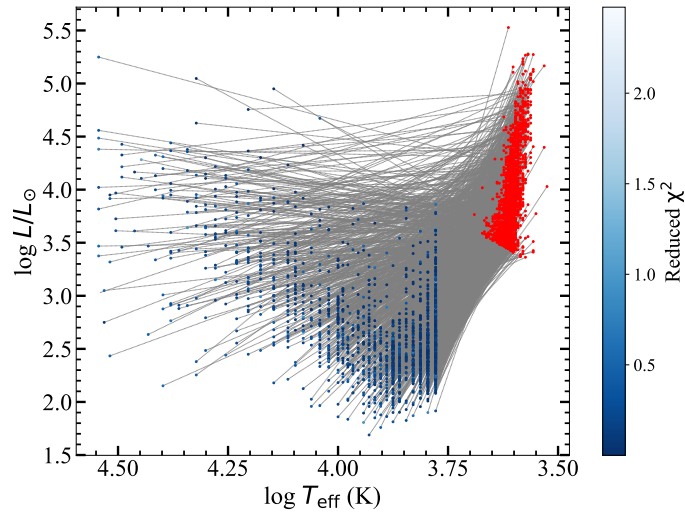


Figure 7. The H-R diagram of all the companion stars (blue dots) and their corresponding RSGs (red dots), gray connecting lines demonstrate the one-to-one correspondence between each stellar pair. The color bar represents the reduced χ^2 of the companion SED fitting.

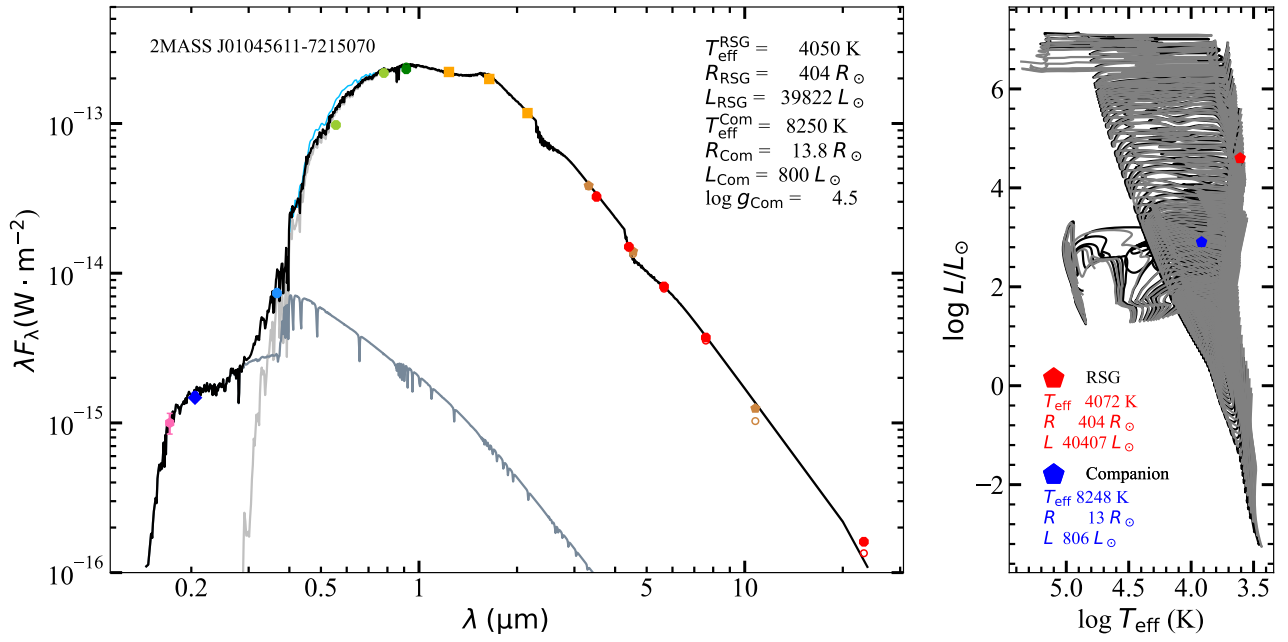


Figure 8. It is similar to the Figure 6, but it is an example of the SED fitting for a "cool" with $T_{\text{eff}} = 8250 \text{ K}$ companion star.

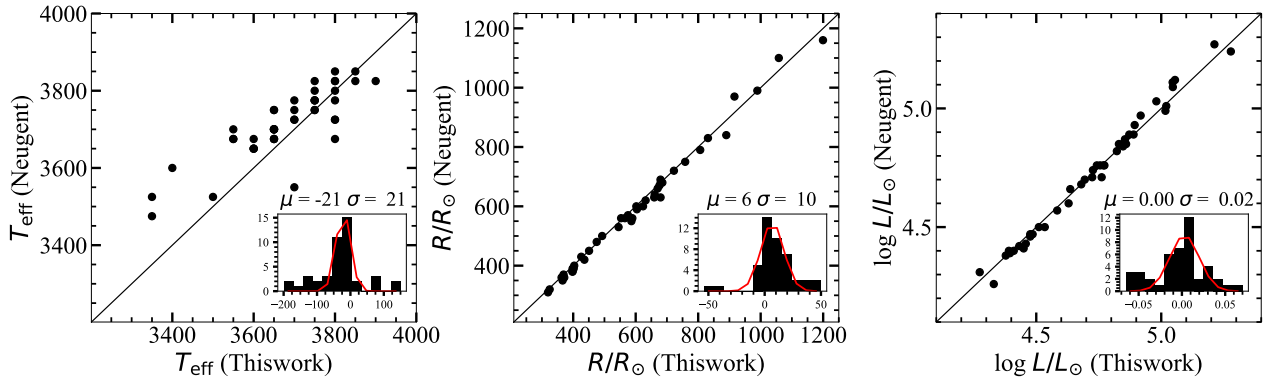


Figure 9. Comparison of T_{eff} , R and L derived from this work and Neugent et al. (2020).

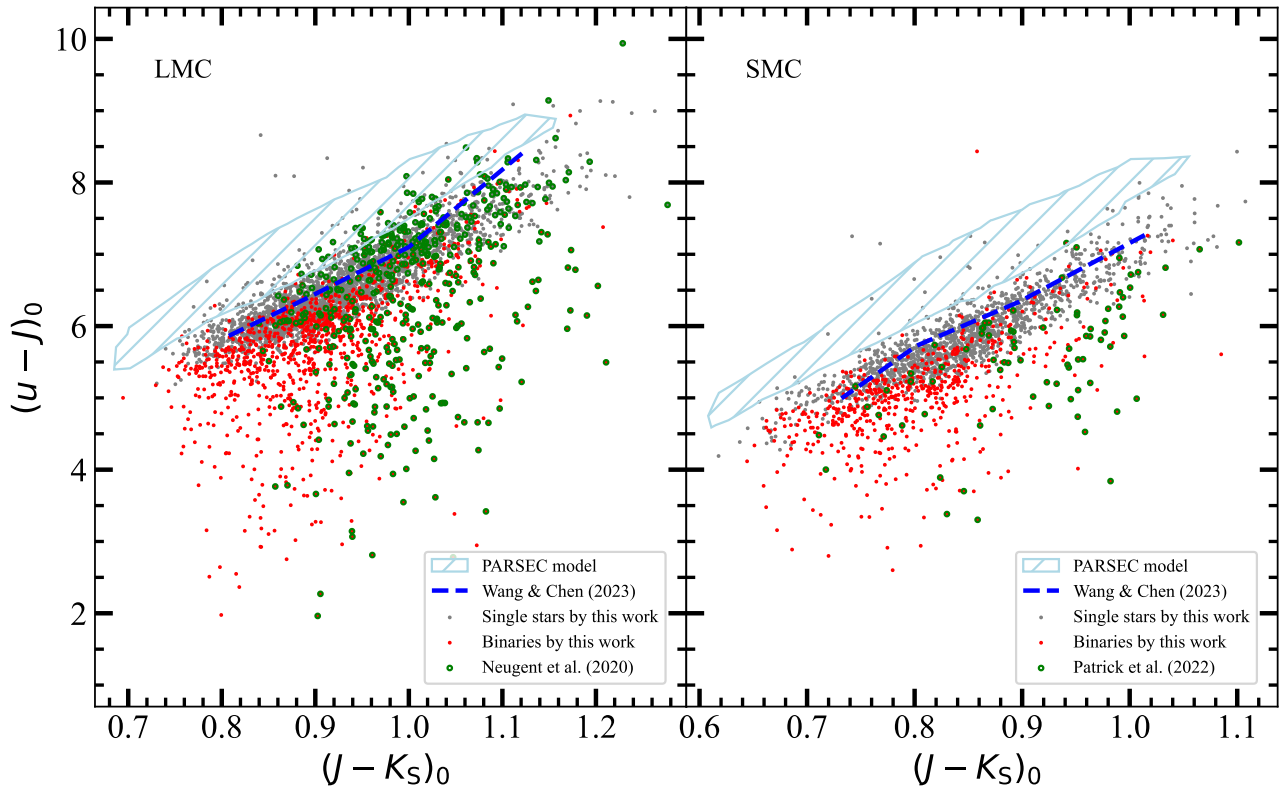


Figure 10. The RSGs sample of this work in the $(u - J)_0$ vs. $(J - K_S)_0$ diagram. The red dots represent the RSG binaries identified by this work, and the green circles represent the RSG binaries identified by [Neugent et al. \(2020\)](#) and [Patrick et al. \(2022\)](#). The gray dots represent the RSG single stars in this work. The region of light blue shaded area represents the location of single RSG stars predicted by the PARSEC model, and the blue dashed line represents the location of RSGs by [Wang & Chen \(2023\)](#).

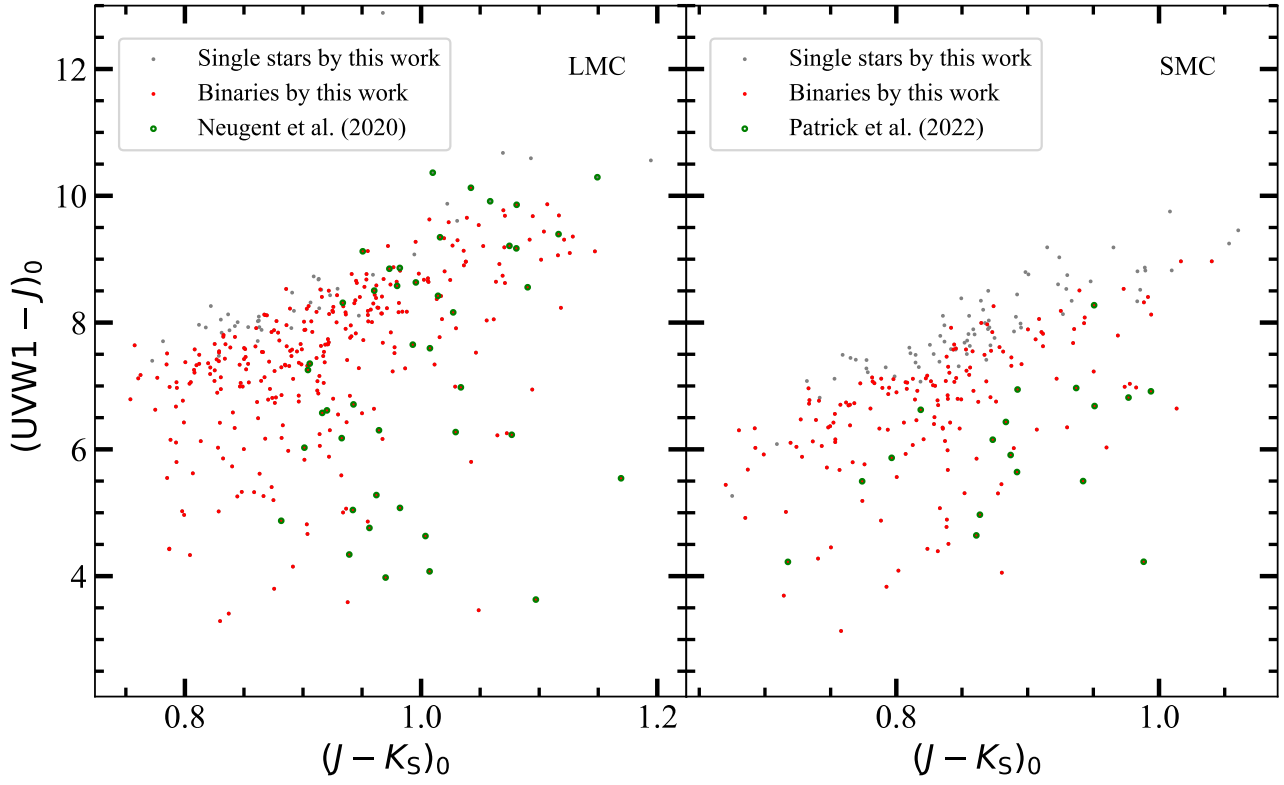


Figure 11. The RSG binaries from the sample of this work in $(UVW1 - J)_0$ vs. $(J - K_S)_0$ diagram. This figure is similar to Figure 10.

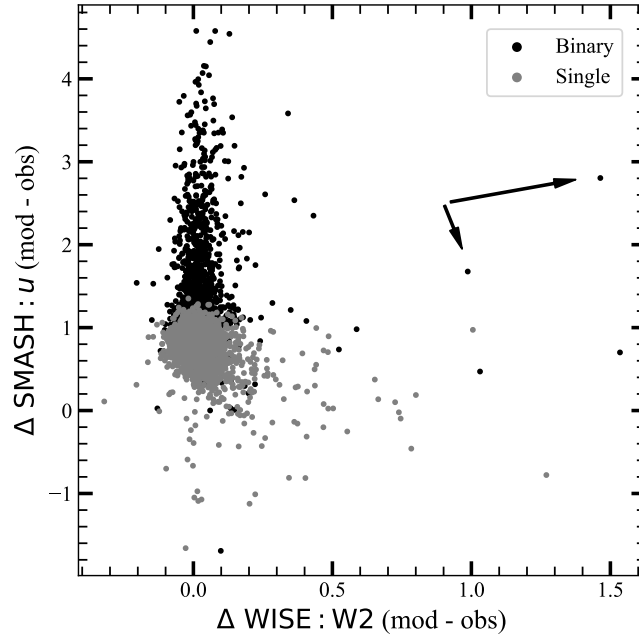


Figure 12. IR excess vs. UV excess diagram. The two stars indicated by black arrows may be affected by circumstellar dust.

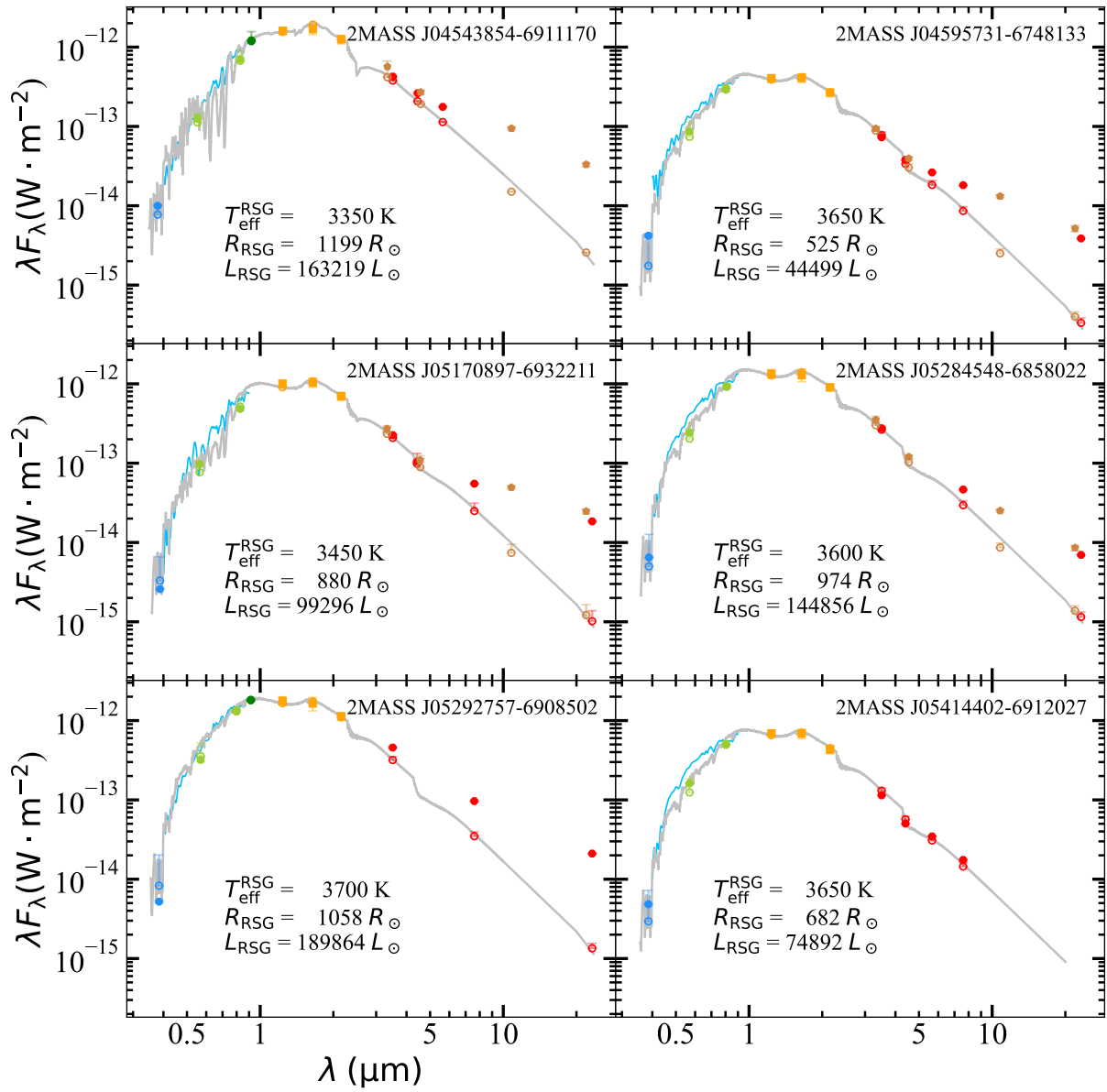


Figure A1. The SED fitting of the RSG component of 2MASS J04543854-6911170, J04595731-6748133, J05170897-6932211, J05284548-6858022, J05292757-6908502 and J05414402-6912027. The symbol conventions follow Figure 4.